Xe⁺ Plasma FIB: 3D Microstructures from Nanometers to Hundreds of Micrometers

T. L. Burnett,[1,2*] B. Winiarski,[1,2] R. Kelley,[3] X. L. Zhong,[4] I. N. Boona,[5] D. W. McComb,[5] K. Mani,[3] M. G. Burke,[4] and P. J. Withers[1]

[1]The Henry Moseley X-ray imaging facility, School of Materials, The University of Manchester, M13 9PL, UK
[2]FEI Company, Achtseweg Noord 5, Bldg 5651 GG, Eindhoven, The Netherlands
[3]FEI Company, 5350 Northeast Dawson Creek Drive, Hillsboro, OR 97124
[4]Materials Performance Centre, School of Materials, The University of Manchester, Materials Department, Manchester, M13 9PL, UK
[5]Center for Electron Microscopy and Analysis, The Ohio State University, 1305 Kinnear Road, Columbus, OH 43212

*timothy.burnett@manchester.ac.uk

Abstract: Xenon plasma focused ion beam (FIB) technology has the potential to investigate large volumes, hundreds of micrometers in size whilst retaining the high resolution of SEM imaging. Three different materials, an aluminum alloy, a zirconium-based metallic glass, and a tungsten carbide-cobalt hard metal, were subject to serial sectioning to build up 3D microstructural images. Lastly a sample of human dentine was shaped into a pillar for analysis using nanoscale X-ray CT. The plasma FIB broadens the range of length scales, which can be investigated and holds significant promise for bringing new understanding of complex microstructures.

Introduction

There is a critical need to analyze many material systems in three dimensions (3D), for example to understand the connectivity of phases, porous networks, and complex shapes. Fortunately, there are now several tools available for 3D characterization, for example, X-ray computed tomography (CT) [1], serial section SEM Tomography (SST) [2–4], transmission electron tomography [4], and atom probe tomography [5, 6], each covering different length scales (see Figure 1).

FIB-SEM SST. The emergence of focused ion beam scanning electron microscopy (FIB-SEM) using a gallium ion FIB has provided a means of accessing volumes of interest (VoI) using SST. The Ga⁺ FIB-SEM is also an important tool for the creation of transmission electron microscopy (TEM) samples. In practice, acquisition times limit the method to volumes about $(50\,\mu m)^3$ for site-specific 3D analysis using SST close to the surface with slice thicknesses down to ~10 nm. Despite its destructive nature, SST enables detailed 3D imaging of phases, grain structure (via electron backscatter diffraction (EBSD)), and chemistry (by energy dispersive X-ray spectroscopy (EDS)) [8]. However there are many cases where it would be of interest to probe large VoIs that are submerged deeper within the sample. In an effort to respond to this challenge, the concept of correlative tomography, the 3D equivalent of correlative microscopy, has been proposed as a way of studying a VoI over multiple scales by coupling X-ray CT and SST to acquire multiple types of data (structural, crystallographic, chemical, etc.) that can be brought into registry for the same region [9].

Plasma FIB. Recently Xe⁺ plasma FIBs [10, 11] have emerged, demonstrating faster materials removal rates compared to Ga⁺ liquid metal ion source FIBs [12]. In this article, we examine the capabilities of a Xe⁺ Plasma FIB (PFIB)-SEM dual-beam system for 3D analysis across a range of materials and applications.

The FEI Helios PFIB used in this study has a maximum current of 1.3 µA compared to a maximum current of ~65 nA for many Ga⁺ FIB systems. In addition to a higher maximum current, which is useful for coarse milling duties, we can operate the PFIB at currents up to 180 nA for the preparation of high-quality cross sections for imaging. In addition, the Xe⁺ PFIB avoids potentially harmful chemical reactions, such as those that can result from Ga⁺ FIB milling [13]. We are continuing to build our understanding of this technology to enable us to apply it to a large range of potential applications. Here we present four example applications where we have successfully applied the PFIB: describing the size of the volumes interrogated, the resolution, and the 3D reconstruction.

Three different serial sectioning results are presented: a stress corrosion crack tip in a 7000 series Al alloy, a Zr-based bulk metallic glass (BMG) with embedded dendrites, and a tungsten carbide hard metal with a cobalt binder phase (WC-11 wt% Co) analyzed by 3D EBSD. A fourth example shows the preparation of a site-specific pillar of human dentine for nanoscale X-ray CT.

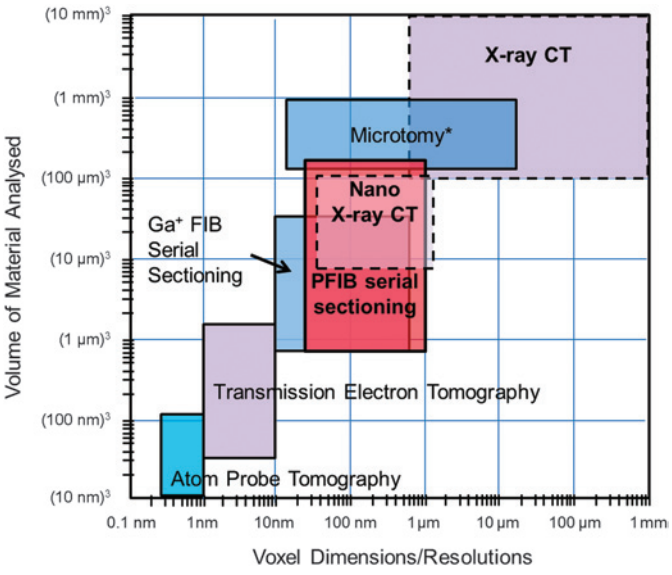

Figure 1: 3D imaging methods for materials science. Non-destructive methods are represented by dashed lines. Microtomy is typically only for soft material [7].

The single source

for all your **specimen coating equipment** and **thin film deposition supplies.**

Cressington 208HR Sputter Coater
Variable Sputter Current & Argon Pressure
High Resolution Coating of 15 Metals + Iridium

Cressington 208C Carbon Coater
High Precision Carbon Rod Coating with
Voltage Controlled Evaporation Source

Rotary Stages
Wide Selection
of Sample Holders

Dual 108 Sputter/Carbon Coater
Independent Operation
Prevents Cross Contamination

208C Accessories
Metal Evaporation, Aperture
Cleaning & Glow Discharge

Sputter Targets
for All Coater Brands

PELCO easiShaper™
Carbon Rod Shaper

TED PELLA, INC.
Microscopy Products for Science and Industry

www.tedpella.com sales@tedpella.com 800.237.3526

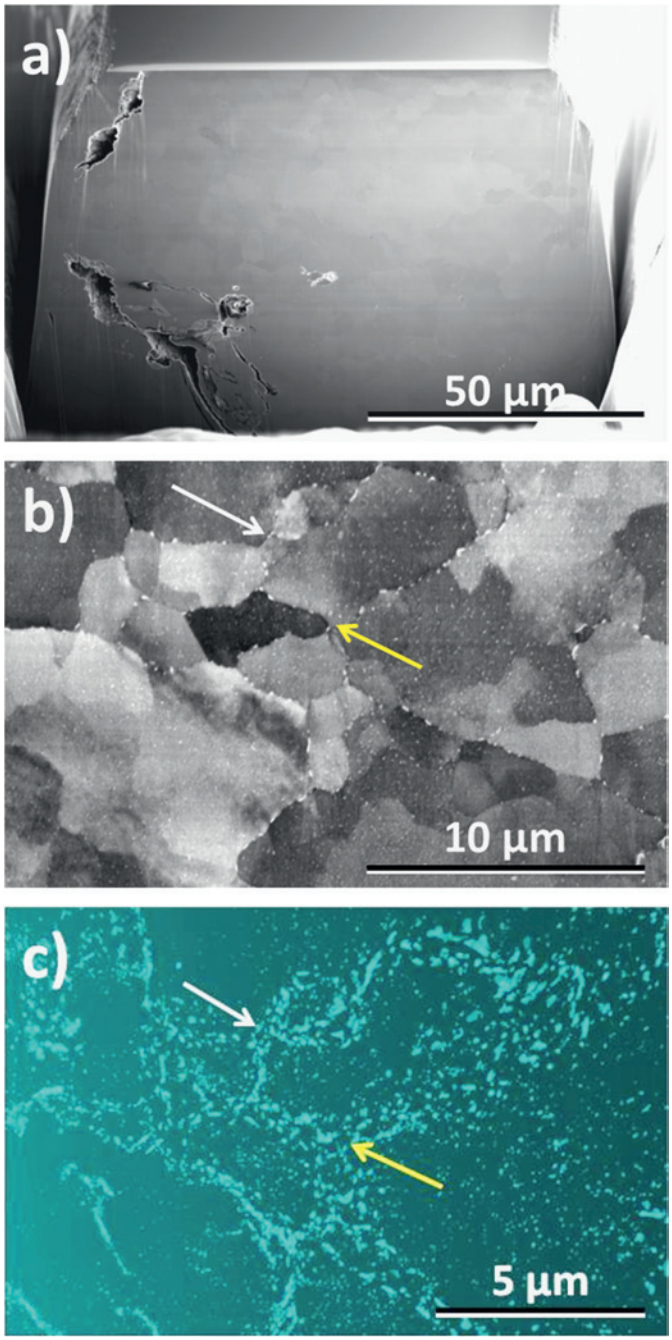

Figure 2: Stress corrosion cracking in a 7000 series aluminum alloy. (a) SEM image of the PFIB-prepared block for serial sectioning showing a part of the stress corrosion crack in the aluminum alloy. (b) Magnified region of a slice showing the detailed microstructure of the aluminum grain structure captured with an 18 nm pixel size. (c) 3D rendering showing precipitates, predominantly along grain boundaries taken from a sub region of (b) and presented at a non-orthogonal angle. Arrows indicate the registration of (b) and (c).

Materials and Methods

Operating conditions. All experiments were conducted using an FEI Helios PFIB operated at 30 kV. For the serial sectioning studies, a current of 59 nA was used within the automated procedure whilst higher currents were employed for the initial shaping of the block for serial sectioning. The FEI Auto Slice and View™ (ASNV) software was used to manage the slicing and imaging process with integrated rocking milling. This method has been developed to minimize curtaining that may arise during unidirectional FIB milling. It uses a stage move to create each alternate slice with the incident ion beam coming from +/- 5° with respect to vertical top-down 0° milling. Details of the setup can be found in [13]. The Nanoscale X-ray CT measurements were made using a Zeiss Xradia Ultra 810 operating at 5.5 kV. All 3D data were aligned, post-processed, and visualized using FEI Avizo 9.0.0 software.

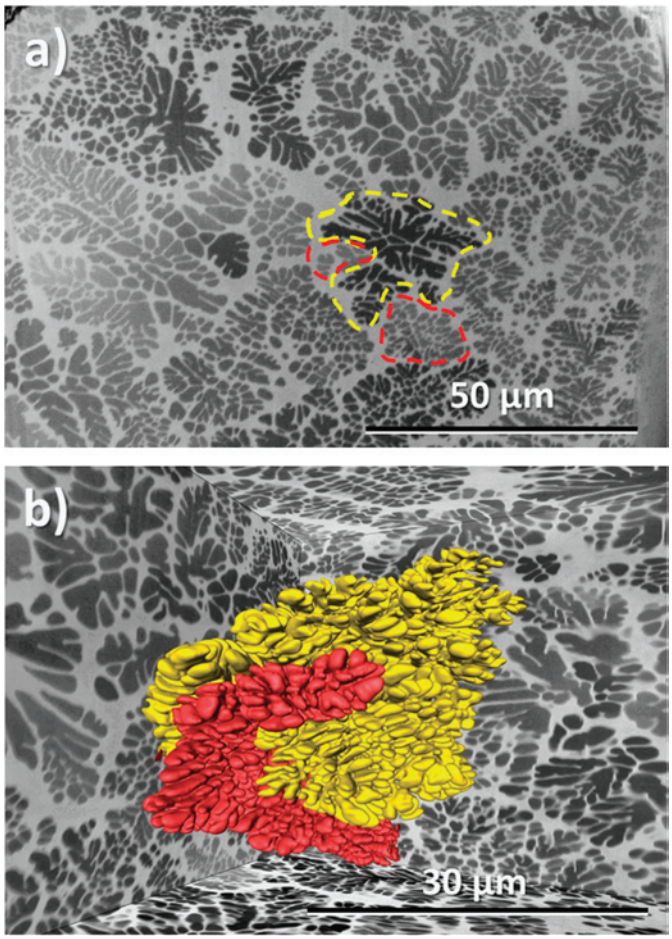

Figure 3: Zirconium-based bulk metallic glass. (a) SEM image of a single PFIB-prepared slice of the Zr-based BMG showing the dendrites. Two interlocked red and yellow grains are highlighted in outline. (b) 3D rendering showing the interlocking of two dendrites of which (a) shows only a section through.

Stress corrosion crack. A stress corrosion crack in a 7000 series aluminum alloy is presented to show the ability to target site-specific locations using the PFIB-SEM. It is only possible to look at a part of this large crack, but it is of sufficient volume to appreciate the morphology at the 100 µm scale and relate it to the complete crack. A 50 nm slice thickness and a pixel size of 16 nm was used in the ASNV software, which was sufficient to observe many of the precipitates in the material and the particles decorating the grain boundaries. This made it possible to look for evidence of an interaction of the crack with these particles as it propagated along the grain boundaries.

Zirconium-based bulk metallic glass. The bulk metallic glass (BMG) sample was analyzed with a 100 nm slice thickness and a pixel size of 24 nm. This is a novel new material with a composition $Zr_{58.5}Ti_{14.3}Nb_{5.2}Cu_{6.1}Ni_{4.9}Be_{11.0}$ consisting of a bulk metallic glass matrix within which crystalline dendrites have grown. This material is being investigated as a high-strength, high-ductility

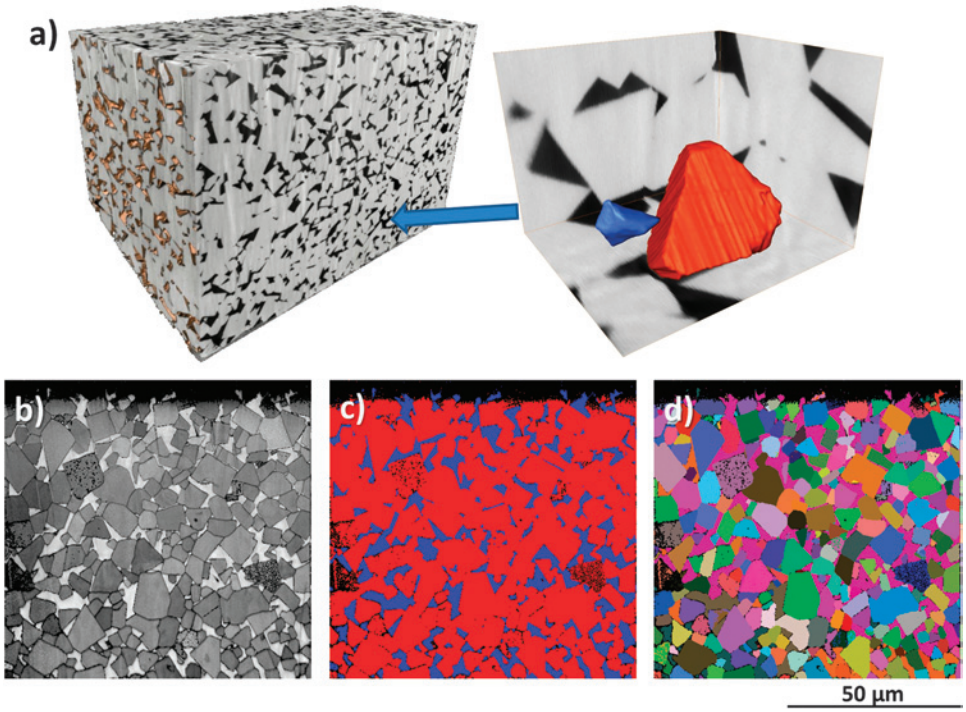

Figure 4: Tungsten carbide WC-11 wt.% Co. (a) Reconstructed volume of 150 × 120 × 80 µm^3, with inset showing zoomed-in details of a facetted WC grain shown for 25 × 25 × 15 µm^3 sub-volume size. Remaining images show EBSD analysis results: (b) band contrast, (c) phase map (WC red, Co-blue), and (d) Euler-colored orientation map.

material. The goal of the analysis was to understand the complex 3D microstructure of this material, in particular the size, morphology, and arrangement of the embedded dendrites. The size of the dendrites in this case was too large for effective observation using the limited volumes accessible using a Ga^+ FIB-SEM.

Tungsten carbide. This material is used in a number of applications where a very hard-wearing surface is required, which includes faces for various cutting tools. The WC-11 wt% Co sample is very challenging to prepare effectively using the Ga^+ FIB, possibly because of some chemical interaction. Therefore images and EBSD maps were recorded from the PFIB-prepared cross sections of this material to assess the quality of results on what is considered a material that is difficult to FIB machine.

Human dentine. Lastly a biological sample of human dentine was prepared for examination with a Nanoscale X-ray CT (NanoCT). This insulating material illustrates a different perspective on the type of work that can be effectively carried out with the PFIB. The time needed to produce a pillar of ~50 µm diameter and ~100 µm height would be practically prohibitive in the Ga^+ FIB. The bulk sample was gold-coated to alleviate charging. Coarse milling was conducted at 30 kV, and a series of milling currents of decreasing magnitude, from 1300 nA to 180 nA, was employed followed by a final shape-defining milling at 59 nA to give a smooth finish. A layer of Pt was deposited on top of the pillar to protect it during machining. Platinum was also used to attach the pillar to the Easylift^{TM} probe for lifting the pillar out of the bulk sample and placing it on the pin sample holder.

Results

Aluminum stress corrosion crack. The results of the ASNV of the stress corrosion crack in the 7000 series aluminum sample are shown in Figure 2. The total volume imaged was 100 × 110 × 12 µm^3, acquired with a total of 241 slices each 50 nm thick. The image pixel size was (16 nm)^2 as recorded using the through-the-lens electron detector (TLD). The total time to collect 1 slice was 3 minutes including 40 s slicing time. Figure 2b shows a magnified region that has been post-processed with an adaptive histogram equalization and median filters. The grains and precipitates are clearly visible. Figure 2c shows a 3D rendering of the precipitates in a small volume of the material. The arrangement of these precipitate particles along the grain boundaries is visible. Many of the smaller intragranular precipitates are visible in the slice images but are typically smaller than the slice thickness of 50 nm, and so they are difficult to label separately. This range of scales (100 µm × 100 µm cross section and the 18 nm pixel size) allows understanding of the meaningful scales of the stress corrosion crack such that the results here can be linked to light microscopy and microscale X-ray CT studies going up in scale to the entire crack. Further details of the microstructure could also be obtained by linking to higher-resolution analysis using fine-scale SEM or possibly TEM analysis. The nature of stress corrosion cracks and the interaction they have with the microstructure demands a 3D understanding.

Zirconium-based bulk metallic glass. The bulk metallic glass sample is shown in Figure 3. The total volume imaged was 120 × 100 × 68 µm^3, a total of 678 separate 100 nm thick slices. The image pixel size was (24 nm)^2 as recorded using the TLD. The total time to collect 1 slice, including slicing and imaging was 120 s. The resulting microstructure is a complex array of dendrites that grow out from a central nucleation point, which is difficult to understand from a 2D section. As shown in Figures 3a and 3b, SST quickly reveals the 3D arrangement of the dendrites within the glass matrix and forms the basis for understanding the microstructure. Again the combination of large volumes (to capture multiple dendrites) with high resolution (to capture the dendrite arms), as well as the strong contrast, necessitates the use of the PFIB-SEM and its capabilities.

Tungsten carbide. Figure 4 shows the microstructure of the WC-11 wt% Co specimen. Two volumes were captured: (1) an ASNV volume 100 × 100 × 80 µm^3 with a total of 800 individual 100 nm thick slices. (2) A 3D EBSD volume 100 × 100 × 3 µm^3, capturing a total of 33 slices at 100 nm thick. The EBSD conditions used were 20 kV and 22 nA, with a step size of 200 nm and a map size of 515 × 530 pixels. The total time to acquire the data for one slice was about 51 minutes: 51 s slicing time and 50 minutes to collect the EBSD map from each slice.

Figure 4a shows a 3D image of the structure. A large number of grains have been captured making these results statistically significant when trying to understand the size

and shape distribution of the WC grains. A practical volume of $(100\,\mu m)^3$ is possible in the PFIB-SEM compared to a typical volume of $(50\,\mu m)^3$ captured in the Ga^+ FIB-SEM. Based on an average grain size in this material of 11.5 µm, determined from the PFIB-SEM dataset, it is possible to capture ~660 grains compared to ~80 grains possible in the Ga^+ FIB-SEM.

This material was specifically chosen for this 3D EBSD study because it has presented significant problems when investigated at a smaller scale within the Ga^+ FIB-SEM. The WC phase is resistant to FIB machining and is difficult to prepare damage-free. Figures 4b to 4d show a series of maps collected from a single slice prepared during an automated EBSD procedure. It has been possible to prepare a large cross section of this material using PFIB at 30 kV and 59 nA with a time of only 51 s to create each new slice. The EBSD results show the indexing rate is over 80%. An issue facing this large-volume EBSD analysis is the time taken to collect the EBSD maps. In this study acquisition of 33 slices took ~30 hours, although it should be noted that much faster acquisition rates would be possible on many other materials such as ferrite, austenite, nickel, copper, etc. with mapping times of less than 10 minutes, depending on the map size and resolution required. The speed and quality of the PFIB cut opens up volumes of real significance, but time has to be spent optimizing the EBSD mapping for maximum speed. Despite the current level of optimization we have achieved, we need further hardware and software developments to alleviate this bottleneck in acquisition of large-volume, high-resolution 3D EBSD datasets.

Preparation of human dentine for X-ray CT. Lastly, by connecting the non-invasive X-ray techniques to the destructive 3D imaging techniques within a correlative framework, there is a need to locate, excavate, and analyze sub-volumes in further detail. As well as providing high-resolution images of volumes, the PFIB promises to be able to excavate regions of interest, for example, creating samples for nanoscale X-ray CT. This is especially challenging for materials science specimens as an ideal sample size (in this case determined by the X-ray energy and their penetration) with a pillar that is 20–100 µm in diameter and approximately 100 µm tall. To achieve this, milling to a depth of over 100 µm is required, as well as a milled radius of the hole equal to the pillar height. These dimensions put this task beyond the practical means of the Ga^+ FIB-SEM. The ability to create these samples from a site-specific location and then create a sample of the desired dimensions makes this an important capability, combining the precision of the cutting with the fast material-removal rate.

Figure 5a shows a pillar of human dentine prepared by the PFIB. This study had two aims: one was the desire to understand better the 3D morphology of the dentine tubules, and the second was to determine the accurate orientation of the tubules with respect to the subsequently prepared TEM lamellae. Understanding the detailed geometry of the dentine tubules at the sub-micron level is exceptionally difficult to appreciate from 2D cross sections. The quality of the NanoCT results was ensured by predicting the X-ray absorption of the sample and then specifically machining a pillar of the required dimensions using the PFIB. Figures 5b and 5c show the results of the nanoscale X-ray CT scan providing a $(120\,nm)^3$ voxel size and the ability to see the tubules and the increased density along the walls of the tubules.

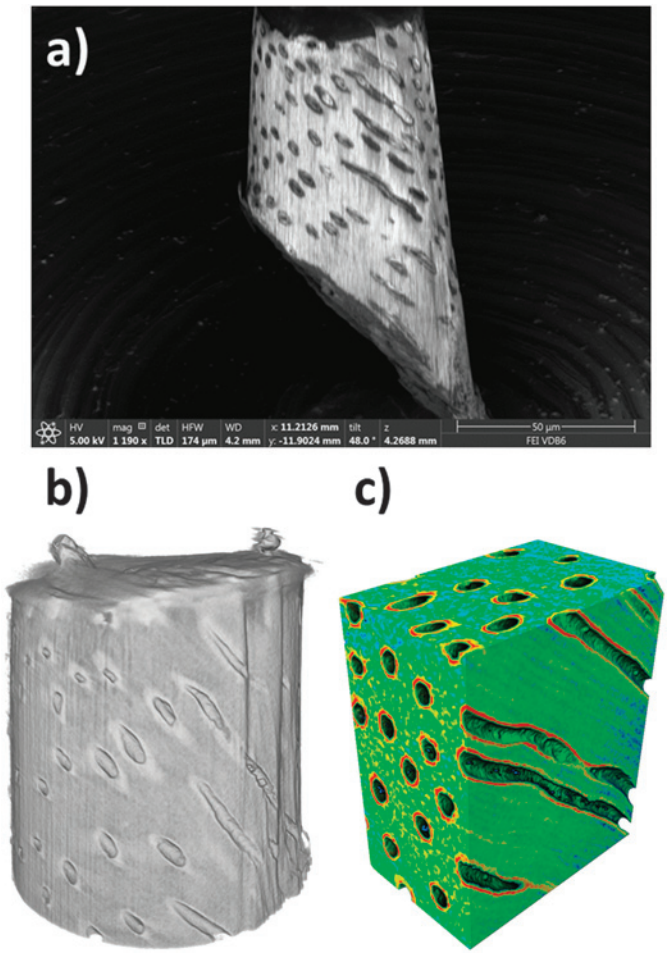

Figure 5: Human dentine. (a) SEM image of the PFIB-prepared dentine pillar attached to the NanoCT holder. (b) 3D rendering of the NanoCT data showing the same orientation of the pillar as the SEM image. (c) Sub-volume showing three orthogonal views of the tubules and the enhanced density material (shown in red) that surrounds the tubules. The final diameter of the dentine pillar was ~45 µm, and the diameter of the dentine tubules was 2–2.5 µm.

Discussion

These results give an overview of some applications where we have successfully applied the PFIB-SEM. The ability to prepare high-quality cross sections at high currents has meant that large volumes can be quickly captured with nanoscale resolution. This is an exciting area for development because many important engineering materials have grain structures many tens of micrometers and can only be characterized effectively over volumes hundreds of micrometers in size. In addition to the results presented here, we have also examined several other materials, including steel, aluminum, zirconium, titanium, alumina, various coatings, and an olivine rock sample. In each case, the parameters had to be optimized. With each new material comes a learning curve to optimize the conditions used. In addition we are continuing to push the

range of materials and operating parameters used to evaluate the true limits of this technology. To date, single cross sections up to 1 mm wide have been produced, and serial-sectioning cross sections up to 300 µm across and 200 µm deep have been fabricated with slice thicknesses 50–500 nm thick.

More work still needs to be done to better understand material interactions with the Xe^+ Plasma FIB. However, in comparison to traditional metallographic preparations of similar materials, PFIB-prepared samples have improved surface quality, yielding EBSD maps and high-resolution images that are essentially artifact-free.

Conclusions

3D data from serial sectioning using the PFIB-SEM across a range of materials suggest that the Xe^+ PFIB can routinely and quickly provide 3D serial section tomographs over dimensions of many hundreds of micrometers whilst retaining nanoscale resolution. This tomographic technique has the ability to capture the rich detail of microstructures, as well as provide analysis by EBSD and EDS. The range of scales available helps bridge the gap between conventional Ga^+ FIB and X-ray tomography for multiscale, multimodal 3D analysis.

Acknowledgements

We acknowledge the EPSRC for grants EP/J021229/1 and EP/M010619/1 and BIS Capital Funding that established the Multidisciplinary Characterization facility. Further authors gratefully acknowledge N. J. Henry Holroyd for the provision for the Aluminum sample, Peter Liaw from University of Tennessee for the BMG sample, and Mark Gee from NPL for the WC-Co sample. DWM would like thank Dr. J. S. Earl, GlaxoSmithKline Consumer Healthcare, for financial support. Our thanks also go to Rene Dobbe, Doug Hahn, and Trisha Rice at FEI Company for their support during this work.

References

[1] E Maire and PJ Withers, *Int Mater Rev* 59 (2014) 1–43.
[2] MD Uchic et al., *MRS Bull* 32 (2007) 408–16.
[3] I Borgh et al., *Acta Mat* 61 (2013) 4726–33.
[4] T Hashimoto et al., *Ultramicroscopy* 163 (2016) 6–18.
[5] C Kübel et al., *Microsc Microanal* 11 (2005) 378–400.
[6] D Blavettea and S Duguay, *Eur Phys J-Appl Phys* 68 (2014) 10101-p1–10101-p12.
[7] TL Burnett et al., *Microsc Microanal* S3 21 (2015) 2003–04.
[8] *Introduction to Focused Ion Beams: Instrumentation, Theory, Techniques and Practice*, eds. LA Giannuzzi and FA Stevie, Springer, New York, 2005.
[9] TL Burnett et al., *Scientific Reports* 4 (2014) 4711.
[10] J Jiruše et al., *Microsc Microanal* S2 18 (2012) 652–53.
[11] L Kwakman et al., *Frontiers of Characterization and Metrology for Nanoelectronics: 2011* 1395 (2011) 269.
[12] NS Smith et al., *J Vac Sci Technol B* 24 (2006) 2902–06.
[13] TL Burnett et al., *Ultramicroscopy* 161 (2016) 119–29.

MT

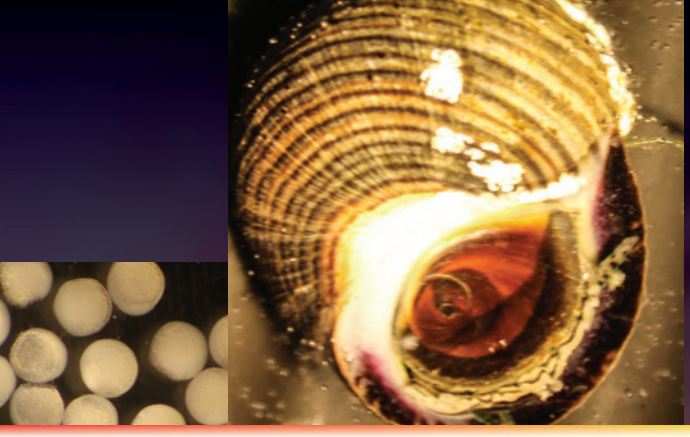

Microscopy + Fluorescence = NIGHTSEA

Fluorescence Viewing Systems

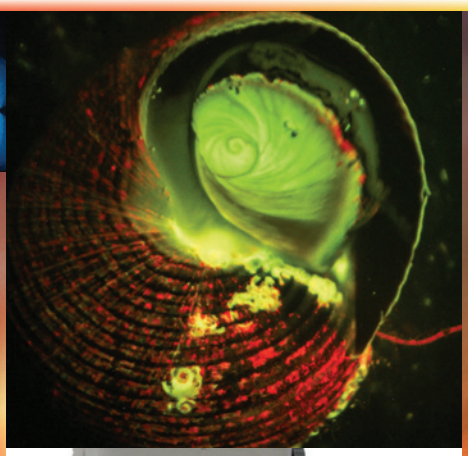

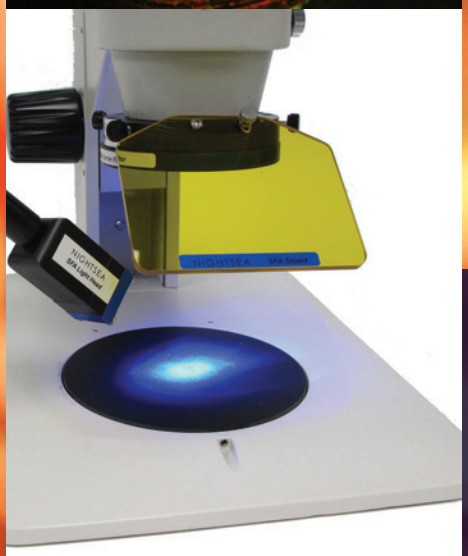

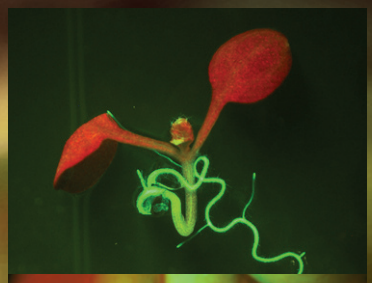

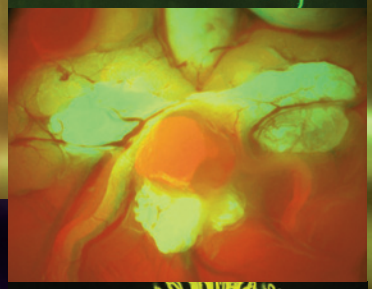

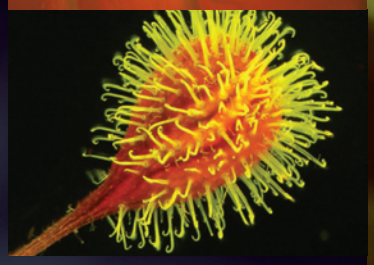

Fluorescence isn't just for research microscopes anymore...

NIGHTSEA™

Stereo Microscope Fluorescence Adapter

Adapt your existing lab stereo microscopes for fluorescence

The NIGHTSEA™ Stereo Microscope Fluorescence Adapter adapts just about any stereo microscope (dissecting microscope) for fluorescence with no modification to the microscope itself. The modular design lets you easily switch between several different excitation/emission combinations to work with a variety of fluorescent proteins and other fluorophores. There are now five different excitation/emission combinations available, plus white light.

Applications

- Quick screening of your fluorescent genotypes — *Drosophila*, zebrafish, *C. elegans*,...
- Genotype sorting
- Fluorescence-aided dissection, injection, or micromanipulation
- Freeing up your research-grade fluorescence microscopes for more demanding work
- New faculty start-up budgets
- Bringing fluorescence into teaching laboratories

CONTACT US FOR MORE INFORMATION...

EMS has it!

Electron Microscopy Sciences

P.O. Box 550 • 1560 Industry Rd.
Hatfield, Pa 19440
Tel: (215) 412-8400
Fax: (215) 412-8450
email: sgkcck@aol.com
or stacie@ems-secure.com

www.emsdiasum.com

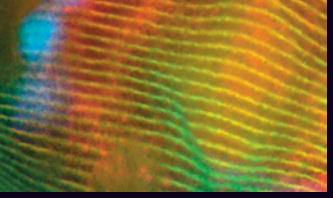

COST-EFFECTIVE 3D IMAGING...

Introducing

Edge® Digital 3D Micro/Macroscopes

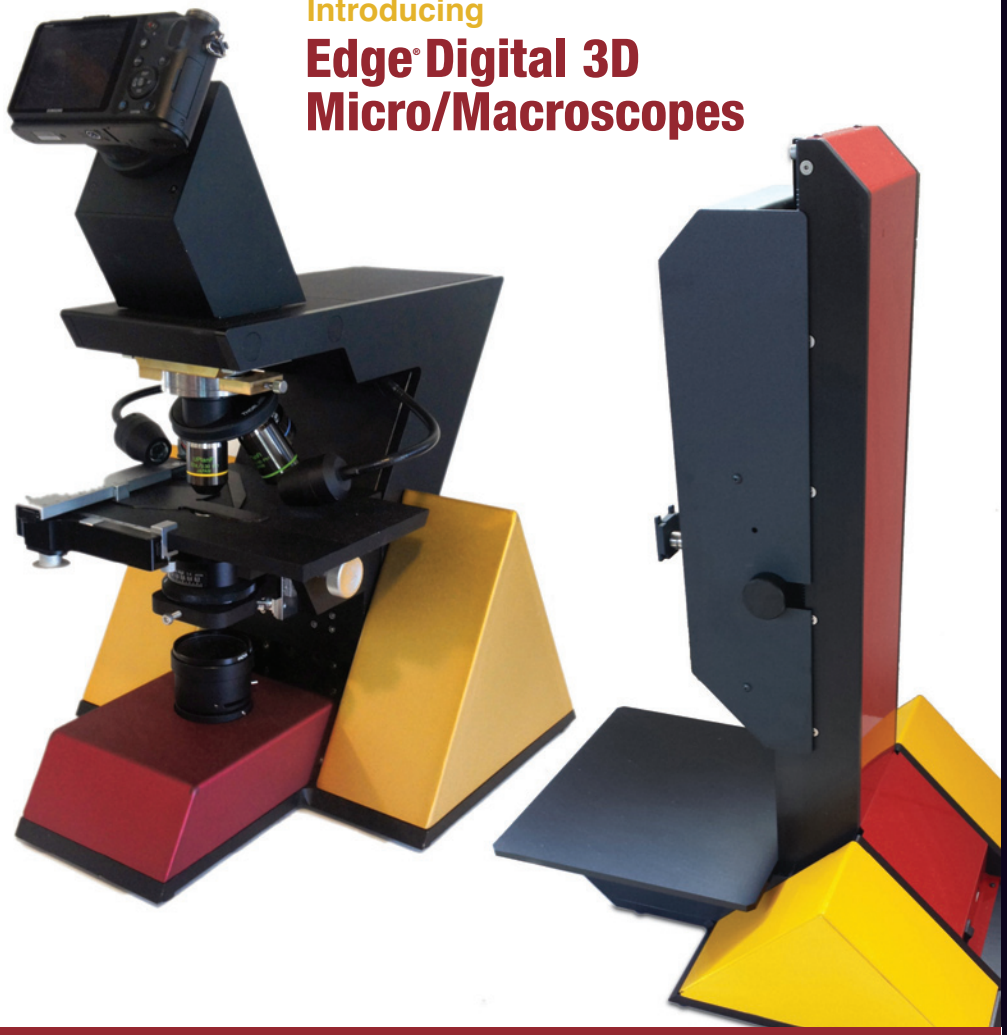

Conventional Microscopes **Edge® 3D Microscope Z-Focus Stacking**

Sample = Golgi Stained Neurons, transmitted light

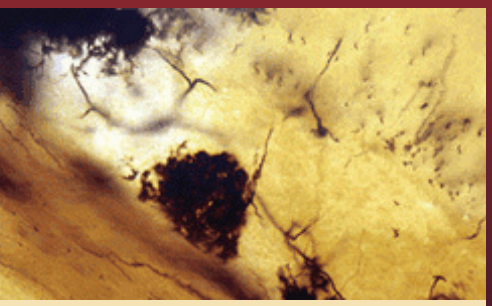

Conventional microscopes only allow you to see small portions of the image in focus at a time.

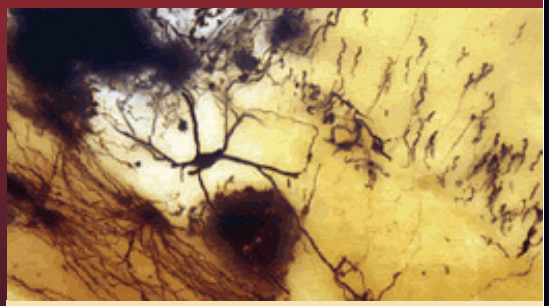

Edge® 3D microscopes allow you to see the entire image in focus with Z-Focus Stacking technology.

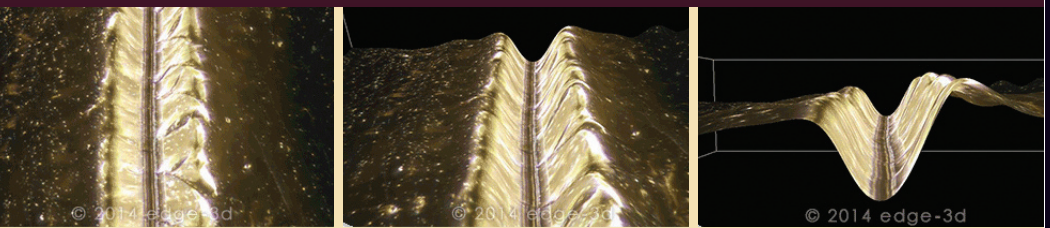

With conventional microscopes it is sometimes very difficult to make clear observations. The Edge-3D microscope's 3D Model mode provides valuable perspective and control to your samples. *Sample = Gold Plate*

EMS has it!

Why 3D?

- The real world is 3D
- Reduce misinterpretation and misdiagnosis
- Increase productivity

Why Edge® 3D?

- Fully automated 3D imaging
- Plug & play and user friendly
- Breakthrough value

Features

- Modes of 3D imaging
  - Stereo 3D using active 3D glasses
  - Stereo 3D using Red/Cyan 3D glasses
  - Motion Parallax 3D Movies (no glasses required)
  - 3D Surface Profiling of Specimens
- Automated Z-Focus Stacking Produces Extended Depth of Focus Images
- Uses Standard Objective Lenses 2X to 100X with Magnifications over 1,000 times
- Transmitted Light
  - Brightfield
  - Darkfield
  - Phase Contract
  - Oblique Illumination and Polarization
- Reflected Light
- Fluorescence Module (coming soon)
- Edge® 3D Panfocal™ Software
  - User Friendly Plug & Play System
    - *Controls the microscope*
    - *Performs 3D image analysis*

CONTACT US FOR MORE INFORMATION...

Electron Microscopy Sciences

P.O. Box 550 • 1560 Industry Rd.
Hatfield, Pa 19440
Tel: (215) 412-8400
Fax: (215) 412-8450
email: sgkcck@aol.com
***or* stacie@ems-secure.com**

www.emsdiasum.com